



1 Imaging and quantification of the 2 pore microstructure of gas shales 3 using X-ray microtomography

4 *Mozhdeh Mehrabi¹, Mehrdad Pasha¹, Ali Hassanpour^{1*}, Paul W.J. Glover² &*
5 *Xiaodong Jia¹*

6
7 ¹Institute of Particle Science and Engineering, School of Chemical and Process Engineering,
8 University of Leeds, Leeds, LS2 9JT, UK

9 ²School of Earth and Environment, University of Leeds, Leeds, LS2 9JT, UK

10 *Corresponding author email, A.Hassanpour@leeds.ac.uk

11

12 Abstract

13 Optimisation of gas production from shale gas reservoirs depends critically upon a good
14 understanding of the porosity and pore microstructure of the shale. Conventionally surface
15 area measurements or mercury porosimetry have been used to measure the porosity in gas
16 shales. However, these conventional methods have limited accuracy and only provide a bulk
17 measurement for the samples. More recently, scanning electron micrography (SEM) and
18 Focussed Ion Beam SEM (FIB-SEM) techniques have been applied in an attempt to address
19 these limitations. Unfortunately, these two methods destroy the samples. In this research
20 three-dimensional x-ray micro tomography (XRMT) imaging techniques were used to capture
21 the structure of three samples and also compared to data from mercury porosimetry. The
22 resulting data have been segmented in order to recognize individual pores down to a
23 resolution of about 1 μm . Distributions of pore volume, pore size, pore aspect ratio, surface
24 area to pore volume ratios and pore orientations were calculated from the XRMT data. It
25 was found that the porosity obtained from XRMT measurements is smaller than that
26 obtained using mercury porosimetry, the reason for which might be displacement of kerogen
27 by the high pressures generated in the mercury technique, but is unlikely to be due to both
28 techniques not being able to measure pores smaller than about 900 nm. Pore volume and
29 size distributions showed all of the shales tested in this work to be multimodal with similar
30 major modal values for volume and pore size. The pores also have a range of pore aspect
31 ratios and surface area to pore volumes, including values indicating the presence of
32 significant oblate spheroidal pores where the major axis is up to 330 times bigger than the
33 minor axis. This has implications both for the connectedness of pores and the resultant gas
34 permeability and the effectiveness of gas desorption processes into the gas shale's pores.
35 These high aspect ratio pores were oriented both in dip and azimuth in preferential
36 directions making it likely that the shale gas itself has significant anisotropy both for
37 permeability and in its mechanical properties. Permeabilities calculated from the XRMT
38 distribution data matched very well with permeabilities obtained by scaling considerations
39 and typical values for similar gas shales.

40

41 **Keywords.** Gas shales, XRMT, anisotropy, porosity, permeability, heterogeneity, mercury
42 porosimetry.

43

44

45



46 1. Introduction

47 Recently research into extracting unconventional resources has increased as oil and gas
48 production from conventional reservoirs continues to decline. Within fifty years it is
49 expected that all hydrocarbon reservoirs will either be small, low permeability,
50 heterogeneous, anisotropic, found in difficult to reach locations, or some combination of
51 these (Miller *et al.*, 2014). Consequently, unconventional reservoirs are becoming an
52 important alternative source of natural gas to meet the huge global demand for energy
53 (Alfred and Vernik, 2012).

54 According to IHS Markit (Edwards, 2015), unconventional reservoirs already account
55 for about two thirds of current global reserves. However, the extraction of hydrocarbons
56 from these extremely low porosity and permeability rocks is extremely difficult. Not only do
57 we not know how much of it we might be able to extract, its extraction requires the use of
58 new techniques and special recovery operations whose cost makes producing these
59 reservoirs often marginally economic and less hydrocarbon prices rise.

60 Unconventional hydrocarbon resources exist in a number of different forms
61 including tight gas and oil reservoirs, coal bed methane deposits and thick formations
62 containing shale gas. This paper focuses on significant shale gas deposits. It recognises that
63 the gas held in shale gas deposits occupies a pore microstructure of which little is known, at
64 least at a microscopic scale. Since it is these rocks that need to be hydraulically fractured so
65 that gas will flow from them, we consider that a better understanding of the microstructure
66 of gas shales will be extremely useful in designing ways to extract more shale gas from them.

67 According to the United States Energy Information Administration (USEIA), 60% of
68 the Earth's sedimentary crust consists of shale, and the organic matter in it is the primary
69 source of all hydrocarbons, as either a gas or oil (Blyth and De Freitas, 1984). Shale is a fine
70 grain sedimentary rock derived from clastic sources and which contains a significant amount
71 of different clays mixed with fragments of quartz and other minerals. The organic material
72 that is deposited with these mineral particles (clasts) is altered by temperature and pressure
73 (Tissot and Welte, 1978) leading to the formation of kerogen and the creation of
74 maturation-induced pore space filled with hydrocarbons. However, these hydrocarbons
75 remain trapped within the shale because of the rock's ultra-low permeability (Alfred and
76 Vernik, 2012). The increased pore pressure created through hydrocarbon generation could
77 also result in maturation-induced micro-cracks (Vernik and Liu, 1997) that may provide
78 increased migration of hydrocarbon into reservoirs, creating the world's conventional oil and
79 gas resources. However, much of the hydrocarbons, remain in the shale source rocks
80 because they occupy and cannot leave a rock microstructure consisting of millions of
81 extremely small and often unconnected pores (Alfred and Vernik, 2013). During production,
82 access to this trapped gas is currently improved by the use of hydraulic fracturing. However,
83 this process is presently a very much hit and miss affair because we do not know how the
84 shale gas is distributed within the gas shale at a microscopic to macroscopic scale
85 (Richardson *et al.*, 2013) and we have limited ability to control and focus the growth of
86 fractures.

87 Improvements to hydraulic fracturing design and proppant technology have already
88 led to a step change in shale gas production rates. Significant improvements have been
89 shown to occur when the hydraulic fracturing takes full account of the mechanical
90 properties of the rocks (Glover *et al.*, 2000), while high aspect ratio fibre and channelized
91 proppant technology (Schlumberger, 2015) has produced up to 20% greater production
92 rates. Further increases in production rates are likely to be possible by designing hydraulic
93 fracturing campaigns that take account of the microscopic distribution of the hydrocarbons
94 within the shale, but for this to be done we also need more information about how the
95 hydrocarbons are distributed within the shale at a microstructural level (Gerke *et al.*, 2013).

96 Up until now, most studies of the pore structure of shale have used mercury
97 injection capillary pressure (MICP) and nuclear magnetic resonance (NMR) measurements



98 (Sondergeld *et al.*, 2010). The mercury technique, though extremely useful in conventional
99 reservoirs, is less relevant in shales since the injection pressures need to be extremely high
100 to mercury penetrate into the rock at all. These higher pressures begin to compress the rock,
101 crushing the pore spaces that the technique is supposed to be probing, and leading to
102 overestimation of capillary pressures together with underestimations of pore size, pore
103 throat size and porosity. Additionally, neither of these techniques provides information
104 about the microstructure of the pores and how they are connected. On the other hand the
105 NMR technique provides some information about the microstructure but suffers from low
106 resolution and cannot measure the connectivity of the pores.

107 Consequently, another approach is needed. The microstructure of shale has been
108 imaged extensively using Focused Ion Beam (FIB) SEM techniques (Chalmers *et al.*, 2012;
109 Loucks *et al.*, 2009; Ambrose *et al.*, 2010; Passey *et al.*, 2010; Schieber, 2010; Sondergeld *et al.*,
110 2010). However, use of the FIB-SEM method to characterize the 3D microstructure of
111 rock is destructive and very time consuming. A better alternative for quantifying pore
112 structure would be to use 3D X-ray tomography because it is non-destructive, fast, and
113 allows the same sample to be scanned repeatedly. Other allied technologies such as NMR
114 scanning (Sondergeld *et al.*, 2010) and Positron Emission Tomography (Ogilvie *et al.*, 2001)
115 suffer from the same low resolution (approximately 1 mm). We are beginning, however, to
116 see the use of X-ray micro-tomography (XRMT) (Iglauer *et al.*, 2013; Panahi *et al.*, 2014;
117 Reipe *et al.*, 2011; Mayo *et al.*, 2015; Peng *et al.*, 2012; 2015) using highly focused X-Ray
118 beams in the laboratory, which can attain resolutions better than 1 micron. Standard X-ray
119 micro-tomography apparatus can attain resolutions down to 760 nm in ideal conditions,
120 which is sufficient to image most pores in shale, while some apparatus can provide
121 resolutions as low as 20 nm.

122 This work describes an X-ray micro-tomography study to image the microstructure
123 of samples of gas shale at a micron-scale in order to characterise the pore structure.
124 Information has been gathered on microstructural parameters such as the location, size,
125 volume, shape, surface area to volume ratio and preferred orientations of pores in order to
126 help understand how the rock was formed, how it acts as a reservoir for gas, how we can
127 improve gas permeability in such rocks, and how, ultimately, we can extract more gas in an
128 efficient manner. We believe that the characterization of gas shale pore structure must lead
129 to improvements in the amount of gas we can extract from a given reservoir.

130 X-ray microtomography like other techniques has some limitations (Blunt *et al.*,
131 2013), including resolution limits, a trade-off between resolution and sample size, and
132 difficulties in segmentation for materials (or phases) with similar densities due to similar X-
133 ray absorption coefficients. However, these limits are more than made up for by the
134 advantage is the technique has over other imaging techniques when it comes to the imaging
135 of gas shales.

136 In this work we have recognized that before characterisation of gas shales requires
137 an even higher resolution than the 900 nm resolution reported here, and we are currently
138 carrying out further imaging with a much better resolution (down to 50 nm), which will be
139 the subject of further publication.

140

141 2. Methodology

142

143 2.1 Samples

144 The samples imaged in this work have a European source, but due to a confidentiality
145 agreement, it is not possible to disclose further details. Associated mercury injection
146 capillary pressure (MICP) measurements have indicated that the porosity varies between
147 2.8% and 10.4%, while X-ray diffraction (XRD) measurements have shown that the samples



148 are composed of 49.2 and 58.3 wt.% clays, 24.2 to 29.4 wt.% quartz and feldspars, 3.7 to 16.1
149 wt.% carbonates and 2.5 to 8.9 wt.% kerogen (Table 1).

150 2.2 Sample preparation

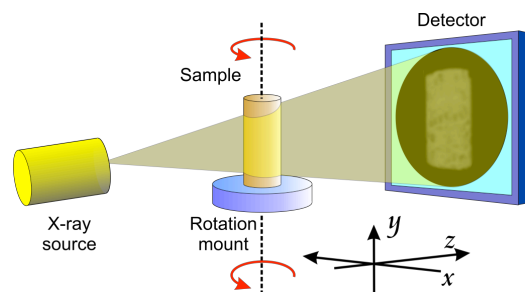
151 In order to optimise the scanning resolution, the sample should be as small as possible and
152 the X-ray source should be brought close to the rotating sample.

153 In this work samples were prepared by taking a small core of shale and cutting it into
154 2 pieces of about 2×1 cm each. Each piece was then mounted on a glass slide (48×26 mm)
155 using thermoplastic wax. In order that the data from different samples can be compared our
156 preparation protocol demands samples are cut into approximately the same size. Each face
157 of the mounted sample was first machined to 1 mm thick using a Buehler PetroThin
158 instrument, turning the sample over and remounting it on the glass slide until a cube of side
159 1 mm was all that remained. Once complete a similar process was carried out on other faces
160 to reduce the sample to a cube of about 500 μm in all dimensions. The thickness of wax
161 between the glass slide and the surface of the sample has been estimated to be 15-20 μm,
162 leading to the corresponding uncertainty in sample size. The samples were finally cleaned
163 with acetone and mounted at the top of a rotating sample holder with cyanoacrylate epoxy.

164 2.3 X-ray Microtomography

165 X-ray micro tomography (XMT) is a non-destructive, relatively fast and accurate technique,
166 which can reveal the internal structure of the shale samples. The technique can be used to
167 scan the sample as many times as needed to visualize internal properties and build a 3D
168 internal structure of the samples (Bakke and Oren, 1997; Li et al., 20010; Curtis et al., 2010;
169 Gelb et al., 2011).

170 The process of X-ray computed tomography (XRMT) consists of taking a number of
171 X-ray radiographs (referred to as projection images) at various angles by projecting an X-ray
172 beam through the specimen and measuring the attenuation of the beam received on a
173 detector (Markowicz, 1993), as shown in Figure 1. Attenuation is quantified in terms of a CT
174 number, with a larger CT numbers being associated with materials have a higher atomic
175 number and density. The projection images are obtained at a large number of different
176 angles as the sample rotates. A technique known as Filter Back-projection (Mersereau and
177 Dudgeon, 1975) can then be used to reconstruct the 3D volume of the specimen.
178



179
180
181

Figure 1. Schematic representation of a computerised micro-tomography measurement set-up.

182 X-ray Microtomography (XRMT) has enough sensitivity to distinguish gas-filled pores
183 from solid kerogen primarily due the large difference in their densities, which leads to a
184 contrast in their CT numbers. In our research the contrast between kerogen and gas-filled
185 pores has been enhanced by adjusting the X-Ray power (*i.e.*, the voltage and current). A
186 simple method for checking whether a pore of crack is gas-filled is to compare the grey-level



187 of the pore or crack with voxels outside the sample. Kerogen mapping will be the subject of
188 a future publication.

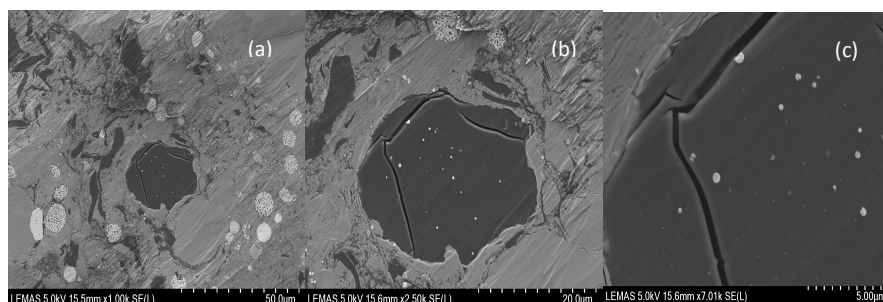
189 Once the 3D volume of the specimen has been obtained, a series of image analysis
190 techniques can be used to visualise the internal structure of the specimen and obtain digital
191 information on its 3D geometry and structural properties.

192 In this study a GE Phoenix Nanotom (XRMT) instrument at the Institute of Particle
193 Science and Engineering at the University of Leeds has been used to obtain the 3D volume of
194 the samples. This apparatus has a microfocus X-ray generator and narrow beam, which
195 allows for the examination of high-density materials such as rocks. The final resolution is
196 determined by the sample size, beam quality and the detector specifications as well as the
197 position of the rotating sample with respect to the beam and the detector. For the samples
198 studied in this research the voxel resolutions of the images were 1.2 μm for Sample 1, 0.9
199 μm for Sample 2, and 1.0 μm for Sample 3.

200 VGStudio software was used to reconstruct the images from projection images and
201 Avizo Fire software was used for image analysis on the obtained volumes. The image analysis
202 provided sample porosity, pore volume, pore aspect ratio, the ratio of the pore surface area
203 to pore volume, the distribution of pore throat sizes, the connectivity of the pores and any
204 preferential directionality (anisotropy) in the pore distribution.

205 2.4 2D SEM Scoping Study

206 To complement this study, samples were also investigated using a scanning electron
207 microscope (SEM) and associated energy dispersive spectroscopy (EDS) imaging. The data
208 acquired in these experiments, allowed identification of the type of minerals and the
209 presence of pre-existing cracks. For example, bright spots in images, often composed of
210 clusters of crystals, as shown in all three panels of Figure 2 indicate pyrite framboids, while
211 fractures are visible clearly.
212



213
214 **Figure 2. SEM image of Sample 2 at (a) 50 μm , (b) 20 μm and (c) 5 μm resolutions. The lightest areas**
215 **correspond to dense material with high atomic number such as pyrite, the darker areas represent low density,**
216 **and low atomic number components such as organic materials, and the darkest regions indicate pores and**
217 **cracks.**

218 3. Results and Discussion

219

220 3.1 Numerical analysis of scan data

221 Figure 3 shows the reconstructed and filtered three-dimensional images from Sample 1.
222 Figure 3(a) shows clearly the complex nature of the microstructure of the shale. There are
223 connected and unconnected pores at all scales and of all aspect ratios as well as pre-existing
224 fractures, again at all scales, some of which may have been the result of sample preparation.
225 In addition there is a complex mixture of minerals including high-density pyrite, which has a
226 high CT number, and shows up at small white small aspect ratio spots.

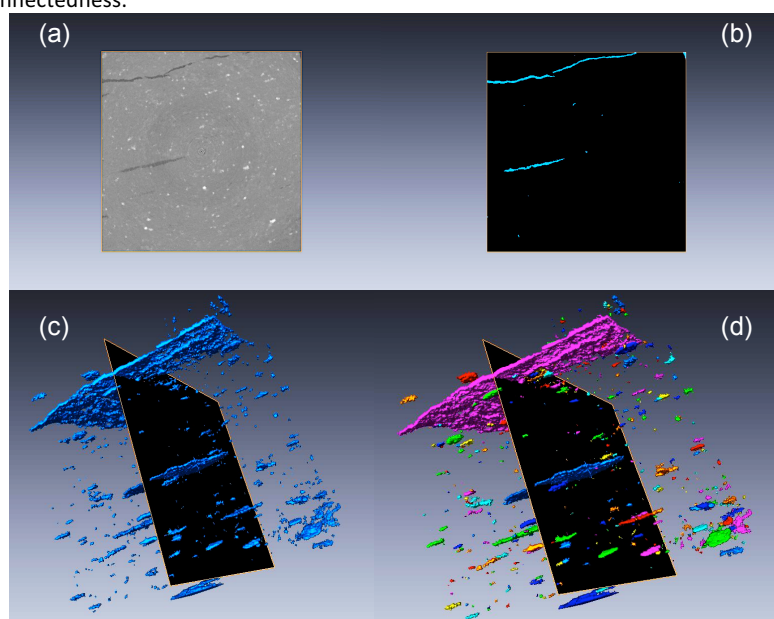
227 The pores were segmented using a defined range of grey values corresponding to
228 gas-filled pores by using manual thresholding, as shown in Figure 3 (b). It is worthwhile



229 noting that most of the pore space is not well-represented in this figure due to the
230 resolution of the figure rather than the resolution of the data.

231 Figure 3(c) and (d) show the three-dimensional pore structures of Sample 1, the
232 pores have been colour coded according to whether contiguous voxels are part of the same
233 pore. In this way each colour represents a fully connected pore. (It should be noted that two
234 clearly separate patches that have the same colour are not connected, but share the same
235 colour simply because of cycling over a limited number of colours in the available palette.)

236 It is possible to analyze the size and spatial distribution of the pore space as well as
237 its connectedness.



238
239 **Figure 3. Image processing workflow, (a) 2D slice of a 0.5 × 0.5 × 0.5 mm volume of Sample 1 using a non-local**
240 **mean filter, (b) the segmented of pore spaces obtained by thresholding with specific range of CT numbers**
241 **(represented by grey-levels) corresponding to pores, (c) 3D volume of pores for the Sample 1, (d) 3D image of**
242 **the connected pores, as the cluster of connected pores are shown in same colour.**

243 Table 1 shows a selection of the most important data from the analysis of the three
244 samples. The most obvious conclusion from the data in Table 1 is that the porosity derived
245 from X-ray micro-tomography is significantly (between 1.5 and 10 times) less than that
246 provided by MICP measurements. This discrepancy is difficult to explain by experimental
247 inaccuracies, and leads to questions over whether use of either the porosity from the MICP
248 technique or the porosity calculated from the micro-tomography is correct in gas shale. One
249 possible cause of the discrepancy is that the fact that the MICP measurement is
250 overestimated due to the high pressures damaging the sample. However, one would expect
251 this to reduce the measured porosity rather than increasing it. Another explanation might be
252 that XRMT at the resolutions available to us are not taking into account pores smaller than
253 our resolution limit (about 900 nm), which would imply that nanopores are extremely
254 important in gas shales. However, these small pores should also be missed by the MICP
255 measurement. Alfred and Vernik (2012; 2013) have recently published a new petrophysical
256 model for gas shales, distinguishing between open porosity and kerogen-filled porosity.
257 Consequently, another source of the apparent discrepancy between the two porosities
258 would arise if the high pressures used in the MICP technique have disturbed the kerogen in
259 the rock samples. This would lead to the MICP measurement returning a porosity composed
260 of the initial gas-filled porosity and some of the space previously occupied by kerogen,



261 leading to an overestimation of the gas-filled porosity of the gas shale. Ward (2010) reported
 262 that the density of kerogen in the Marcellus shale varies with thermal maturity in the range
 263 1.53 to 1.79 g/cm³. If we take a mean density of 1.65 g/cm³ for kerogen and 2.7 g/cm³ for
 264 the other solid components of the rock, we obtain kerogen values of 3.93% by volume for
 265 Sample 1 and 3 and 12.56% for Sample 2. Clearly, there is ample scope for the process
 266 proposed by Alfred and Vernik to occur. If such a process does occur, it would be extremely
 267 important to know what technique was used to measure the porosity of gas shale from a
 268 hydrocarbon potential point of view. Furthermore, comparison of porosity measurements
 269 using two different techniques would possibly allow the fraction of kerogen in the rock to be
 270 determined.
 271

Parameter	Unit	Sample 1	Sample 2	Sample 3
Composition				
Clays		49.2	58.3	49.2
Quartz & feldspar	w.t%	29.4	24.2	29.4
Carbonate		16.1	3.7	16.1
Kerogen		2.5	8.9	2.5
Porosity from MIP	(-)	0.104	0.028	0.104
Pore voxels count	(-)	633	100	258
Total voxel count	(-)	10 ⁹	10 ⁹	10 ⁹
Spatial resolution (voxel size)	(μm)	1.2	0.9	1.0
Voxel volume	(μm ³)	1.73	0.73	0.82
Porosity from microtomography	(-)	0.0071	0.0029	0.0096
Volume of smallest pore	(μm ³)	13.8	2.19	4.6
Volume of largest pore	(μm ³)	5.97×10 ⁶	9.96×10 ⁴	2.47×10 ⁵
Mean pore volume	(μm ³)	1.85×10 ⁴	7.32×10 ³	3.19×10 ³
Median pore volume	(μm ³)	6.15×10 ²	1.32×10 ³	7.28×10 ²
Effective pore radius	(μm)	1.43	1.33	1.42
Formation factor	(-)	2.8×10 ⁶	41×10 ⁶	1.13×10 ⁶
Estimated permeability	(nD)	92.3	5.5	22.3

272 **Table 1. Porosity, pore microstructure and estimated permeability parameters associated with three samples**
 273 **of shale gas measured in this work.**

274 3.2 Pore size and pore volume distributions

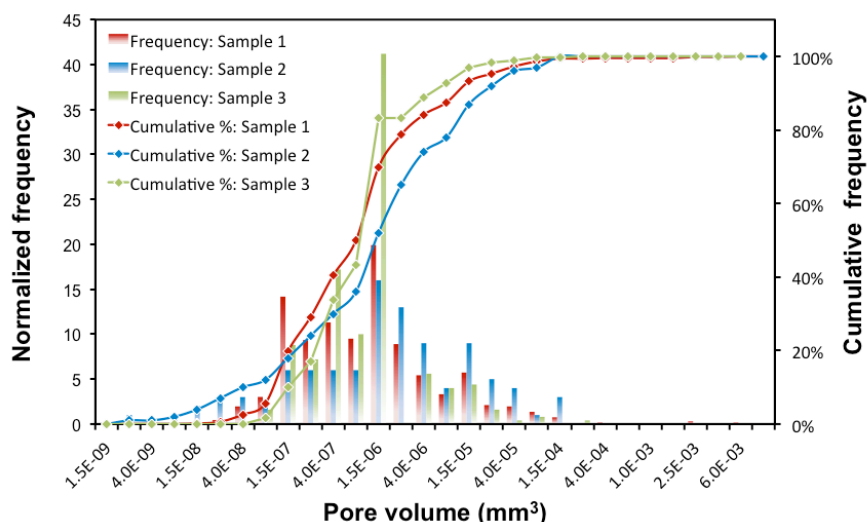
275 The pore volume distribution for each sample is shown in Figure 4 and can be seen to cover
 276 an extremely wide range, from the resolution of the technique in Sample 2 (900 nm) to
 277 about five orders of magnitude higher. Figure 4 shows both the incremental and cumulative
 278 distribution of pore volumes for each of the three samples. It can be seen that pore volumes
 279 range from below 2×10⁻⁹ mm³ to over 2×10⁻⁴ mm³. For these three samples all pore volume
 280 distributions are multimodal but the largest contribution to pore volume in all three samples
 281 occurs at a pore volume of about 1.5×10⁻⁶ mm³, accounting for about 18% of the total pore
 282 volume for Sample 1, 21% for Sample 2 and 41% for Sample 3 by pore number count.

283 The lower limit of the distribution measured in this work is controlled by the
 284 resolution of the technique, with samples 1 and 3 showing a marked reduction in measured
 285 pores with volumes less than 1.5×10⁻⁸ mm³, and 2.5×10⁻⁹ mm³ for Sample 2. The multimodal
 286 character of the distributions hints that there may be significant pore volume in the form of
 287 pores with sizes less than the resolution of the XRMT technique.

288 The upper limit to pore sizes in Sample 2 and Sample 3 is about 1.5×10⁻⁴ mm³ and
 289 2.5×10⁻⁴ mm³, respectively, while for Sample 1, with the presence of a one large crack, it is
 290 6×10⁻³ mm³.



291 The cumulative distributions in Figure 4 show that Sample 1 and Sample 3 have
 292 consistently higher pore volumes than Sample 2 despite the similarity apparent in their
 293 associated incremental pore volume distributions.
 294
 295

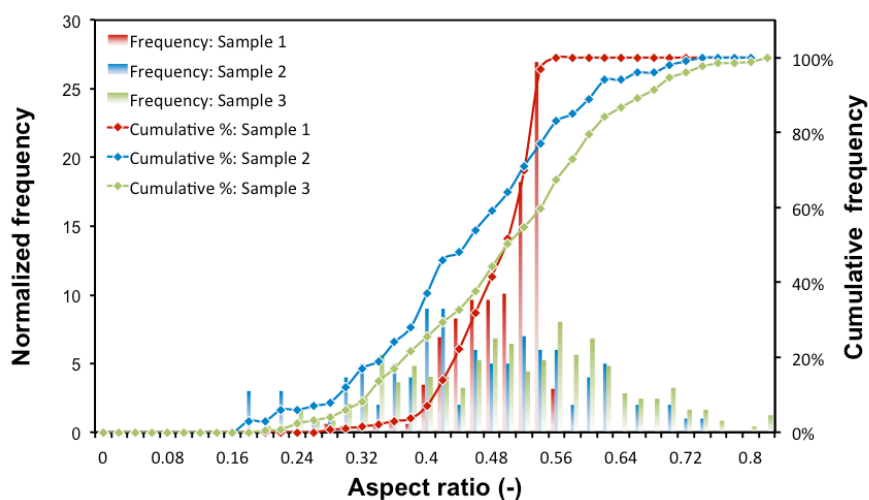


296
 297
 298

Figure 4. Incremental and cumulative pore volume distribution for Sample 1 (Red), Sample 2 (Blue) and Sample 3 (Green).

299 3.3 Pore aspect ratios

300 Pores can be considered to approximate to an ellipsoid with radii a , b and c in each of the
 301 three orthogonal directions x_1 , y_1 and z_1 , where x_1 is taken along the maximum length of the
 302 ellipsoid, y_1 along the next largest, and z_1 along the smallest ellipsoidal dimension. Aspect
 303 ratios can then be described as the ratio of pairs of each of these orthogonal lengths. In this
 304 work we calculate the aspect ratio of two largest bounding box dimension of pores, which is
 305 given by the ratio a/b , where $a \geq b \geq c$. Feret's diameter (Merkus, 2009) was used to calculate
 306 the values of a and b for each pore from the numerical data set.
 307



308
309
310

Figure 5. Aspect ratio distributions for the shale gas samples for Sample 1 (Red), Sample 2 (Blue) and Sample 3 (Green).

311 Pore aspect ratio is a very important parameter in the characterisation of gas shales
312 because it is not only related to the connectedness of the pores (Glover, 2009), which
313 influences the electrical and fluid transport properties of the rock, it is also related to how
314 effectively matrix-bound and kerogen-bound gas can diffuse into the shales pore spaces.
315 High aspect ratios provide more grain-to-grain contact, thus decreasing the pore
316 compressibility (Saleh and Castagna, 2004). Although not evaluated in routine or special core
317 analysis, the aspect ratio distribution of a rock affects the connectedness and tortuosity of
318 pore spaces, which control formation factors, cementation exponents, saturation exponents
319 and ultimately permeability.

320 Figure 5 shows that there is a well-defined preferred aspect ratio that is shared by
321 all samples (0.54, 0.42 and 0.56 for Sample 1, 2 and 3, respectively). However, Sample 2 and
322 3 contain pores with a much wider distribution of pore aspect ratios than Sample 1,
323 indicating that while Sample 2 and Sample 3 contain some pores which are almost spherical
324 as well as others which are very crack-like, together with all shapes in between, Sample 1
325 contains only pores in the middle range, which are never near-spherical nor very crack-like.
326 In fact, Sample 1 has a well-defined maximum pore aspect ratio of 0.56. The implication is
327 clear; some gas shales contain more high aspect ratio pore spaces at a microscopic scale.
328 These high aspect ratio pores are more likely to interlink and will be more likely to give these
329 shales a larger natural permeability. Consequently, we ought to be searching for gas shales,
330 which have high aspect ratios in order to take best advantage of any natural permeability
331 that is present.

332

333 3.4 Pore surface area to volume ratio

334 The shape of each pore also affects its surface area to volume ratio, ξ . This ratio is important
335 because large surface areas facilitate the diffusion of gas initially trapped in the matrix of the
336 rock and in the kerogen into the pore spaces within the shale. This is a necessary step before
337 hydraulic fracturing can open up access to these small pore spaces. A high surface area
338 ensures that the diffusion process is more efficient, not only ensuring a good initial charge of
339 gas in the micro-pores of the shale, but also allowing those pores to be recharged quickly
340 once initial production has removed the initially accumulated gas.



341 Surface areas to volume ratios are best understood by assuming the ellipsoidal
 342 pores to be spheroids of either oblate or prolate types. Oblate spheroids have semi-axis sizes
 343 according to $a=b>c$, i.e., spheres squashed in the c -direction, and approximate to penny-
 344 shaped cracks or pores. Prolate spheroids have semi-axis sizes conforming to $a>b=c$, i.e.,
 345 spheres stretched in the a -direction, and approximate to needles. The volume of both types
 346 of spheroid can be calculated using the formula

$$347 \quad V = \frac{4}{3}\pi abc. \quad (1)$$

348 The surface area of the two types of spheroid differ slightly. They are

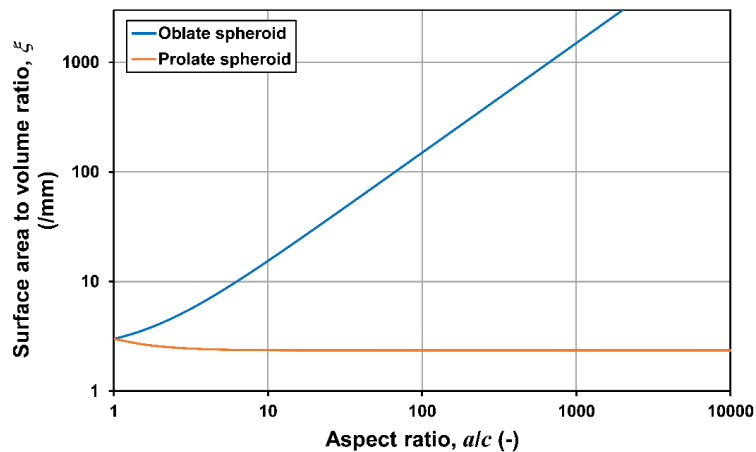
$$349 \quad S_{oblate} = 2\pi a^2 \left(1 + \frac{1-e^2}{e} \tanh^{-1} e\right), \text{ where } e^2 = 1 - \frac{c^2}{a^2} \quad \text{and} \quad (2)$$

$$350 \quad S_{prolate} = 2\pi a^2 \left(1 + \frac{c}{ae} \sin^{-1} e\right), \text{ where } e^2 = 1 - \frac{a^2}{c^2}. \quad (3)$$

351 The surface area to volume ratio for each type are then

$$352 \quad \xi_{oblate} = \frac{3}{2c} \left(1 + \frac{1-e^2}{e} \tanh^{-1} e\right), \text{ and} \quad (4)$$

$$353 \quad \xi_{prolate} = \frac{3}{2c} \left(1 + \frac{c}{ae} \sin^{-1} e\right). \quad (5)$$



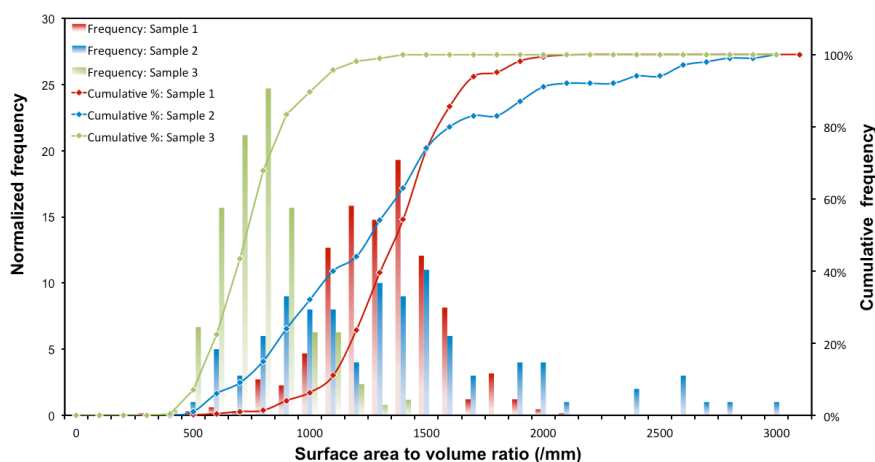
362 Figure 6. Surface area to volume ratio as a function of aspect ratio for oblate and prolate spheroids,
 363 approximating to penny-shaped and needle-shaped pores, respectively.
 364

365

366

367

368 Figure 6 shows the relationship between the surface area to volume ratio ξ of
 369 oblate, penny-shaped pores and prolate, needle shaped pores to their respective aspect
 370 ratios. It is clear that oblate pores provide a much greater surface area per volume than their
 371 respective prolate pores. The XRMT data shows that the pores in the three samples we have
 372 measured in this work are oblate with an aspect ratio of about 0.5, as shown in Figure 5.
 373 However, Figure 5 shows that aspect ratios as high as 0.84 and as low as 0.16 are also
 374 present.



375
376
377

Figure 7. Surface area to volume ratio distributions of the pores. Sample 1 (Red), Sample 2 (Blue) and Sample 3 (Green)

378

379 Figure 7 shows the surface area to volume (ξ) distributions for the three samples
380 measured in this work. Samples 1 and 2 are similar with the ξ ratio varying from about 500
381 /mm to values higher than 2000 /mm and similar modal values at about 1400 ± 100 /mm and
382 1500 ± 100 /mm, respectively. Sample 3 is clearly different, varying from about 500 /mm to
383 values no higher than 1400 /mm with a modal value at about 900 ± 100 /mm.
384

385 The minimum surface area to volume ratios measured for all samples ($\xi=500$ /mm)
386 corresponds, according to the analysis in Figure 7, to an a/b aspect ratio of about 330. In
387 other words, the penny-shaped pore is 330 times wider than it is thick. Likewise, the
388 maximum values of surface area to volume correspond to penny-shaped pores more than
389 1500 times wider than they are thick, with a modal behaviour for Sample 1 and Sample 2
390 showing a/b aspect ratios of about 1000 and about 500 for Sample 3. The implication for gas
391 production is clear; Sample 1 and Sample 2 have twice the surface area than Sample 3 for
392 the diffusion of gas into the pores from the matrix, and these gas shales are likely to provide
393 better long-term resource than that represented by Sample 3 even though, the higher
394 porosity in Sample 3 will likely make it the better short-term prospect.

395 The surface area to volume ratio is also important in other respects. As indicated
396 previously, high aspect ratio and high surface area to volume pores are much more likely to
397 connect up with each other and therefore they are important in defining the natural
398 permeability of the shale. In this regard, Sample 1 and Sample 2 would be expected to have
399 a higher permeability than Sample 3. This is investigated later in this paper.

400 The shape of pores also is the importance in defining the geo-mechanical properties
401 of the rock. Shales have a tendency to plastic behaviour so any tendency to weakness is
402 likely to result in the closure of fractures and pores. High aspect ratio, high surface area to
403 volume penny-shaped pores and cracks are much more prone to closure than those with low
404 aspect ratios and low surface areas to volume (Glover et al., 2000; Curtis et al., 2010).
405 Consequently, though high aspect ratios and high surface areas are beneficial for gas
406 production they are also likely to be found in shales which are difficult to produce from
407 because induced fractures will be more prone to closure in the long-term.

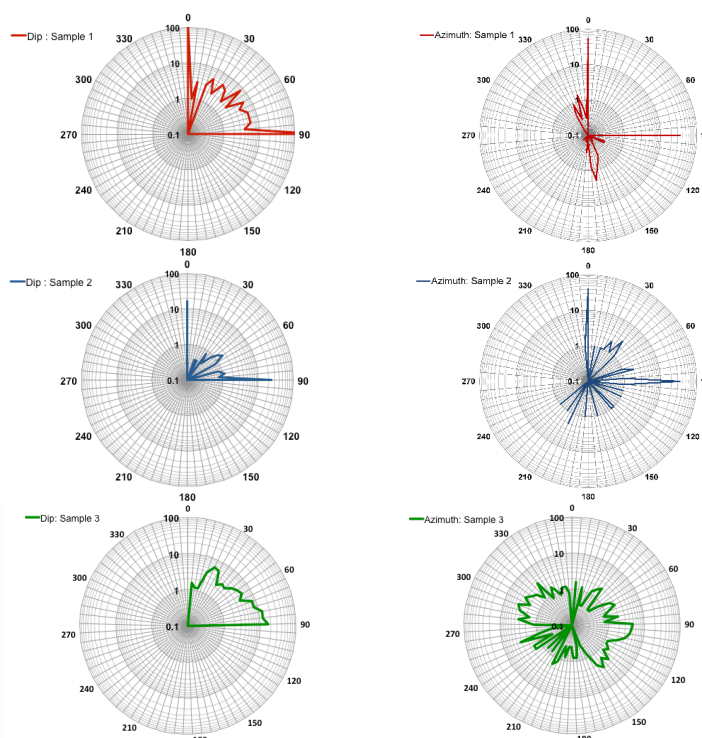
408 The previous analysis assumes that the pores behave like perfect smooth-surfaced
409 spheroids. Of course this is not the case in the pores as can be readily seen in Figure 3. The



410 presence of rough surfaces on the pore walls increases the surface area to volume ratio
411 above that which would be expected by the overall aspect ratio of the pore. It has been
412 known for some years that not only pore size but also pore and fracture surfaces are fractal
413 (Nolte et al., 1989; Bahr, 1997; Ogilvie et al., 2006), and fractal pores can in principle have a
414 surface area to volume ratio that is infinite. Consequently, it should be considered that some
415 samples might have much higher surface areas due to the roughness and of their surfaces,
416 which do not increase the pore volumes but provide much larger pore surface areas.
417 Approaches that take into consideration the fractal distribution of properties such as
418 porosity and grain size are now being implemented in new reservoir modeling approaches
419 and used to create fractal permeability models for shale gas flow (e.g., Geng et al., 2016; Li
420 et al., 2016).

421
422

423



424

425

426

427

Figure 8. Rose diagrams of Dip and Azimuth of the long axis of pores for each of the samples studied. Sample 1 (Red), Sample 2 (Blue) and Sample 3 (Green).

428

429 3.5 Pore orientation

430 The XRMT data can also be analysed to ascertain the orientation of the pores according to a
431 polar co-ordinate system (Figure 8 shows the dip θ ($0 - 90^\circ$) and azimuth φ ($0 - 360^\circ$) of the
432 major axis of the pores for each sample as a rose diagram. It is immediately clear that the
433 Sample 1 and Sample 2 are rather similar, showing marked preferential dips near 0° and 90° ,
434 which is parallel to the tomographic stage and also to the macroscopic bedding observed in
435 the samples. However, Sample 3 has preferential directions between 30° and 80° . In
436 addition Sample 1 and Sample 2 show marked preferential azimuthal directions which are
437 orthogonal at 0° and 90° with additional secondary directions of which the two strongest are



438 $170\pm 5^\circ$ and $34.5\pm 5^\circ$ for Sample 1 and $35\pm 15^\circ$ and $70\pm 3^\circ$ for Sample 2. Overall it is Sample 1
 439 that exhibits greater anisotropy, and this can be seen in the 3D image in Figure 3(c-d).

440 3.6 Permeability

441 The permeability of a rock may be estimated using the pore surface area to volume ratio ξ . It
 442 is well known that the mean effective pore radius can be calculated using the (Johnson et al.
 443 1986) approach, where the effective pore diameter $\Lambda = 2V_p/S_p$, where V_p is the pore
 444 volume and S_p is the pore surface area. Consequently, $\Lambda = 2/\xi$. The Λ -value is a measure of
 445 the aperture for fluid flow which controls the permeability of the sample according to the
 446 relationship $k = \Lambda^2/8F$, where $F = \phi^{-m}$ is the formation factor of the rock (Glover, 2015).
 447 In this equation the value of Λ describes the size of the opening between the rock grains
 448 allowing the passage of fluids, while the formation factor contains the information about
 449 how connected or tortuous those fluid flow pathways are (Glover, 2009; 2010). The
 450 formation factor was not measured directly in this work. However, since the cementation
 451 exponent m for shales varies between about 2.34 and about 4.17 (Revil and Cathles, 1999), it
 452 is reasonable to assume a value of $m=3$. The formation factor can then be calculated using
 453 the measured porosity for each sample.

454 The permeability for each sample can then be calculated, and is found to be 92.3 nD,
 455 5.49 nD and 22.3 nD for samples 1, 2 and 3, respectively (Table 1), which is in agreement
 456 with recent up-scaled permeability determinations for the Barnett shale (Peng et al., 2015).
 457 It is worth noting that Sample 3 does not have a larger permeability than Sample 1 despite
 458 having a larger porosity, which we ascribe to Sample 3 having a smaller surface area to
 459 volume ratio that has not been compensated for completely by the larger porosity of Sample
 460 3.

461 The dimensions of the interconnected pores have a major role in our estimation of
 462 permeability and hence a viable theoretical method to find out effective pore radius or the
 463 size of opening between the rock grains is required. In order to validate the previous
 464 permeability calculations, ImageJ software has been used on SEM images of Sample 2 to
 465 measure the equivalent circular diameter of a crack, which is similar to the measured mean
 466 effective pore radius of same sample.

467 Figure 10 shows an SEM image of Sample 2 with a large crack. The crack has a length
 468 of approximately 19 μm , and is approximately 0.3 to 0.5 μm wide. The equivalent diameter
 469 (Jennings et al., 1988) of that crack has been calculated with the following equation, and the
 470 value can then be compared with the effective pore radius of Sample 2 from Table 1.

471

472

$$473 d_e = 1.3(ab)^{0.625}/(a+b)^{0.25},$$

474

475 where; d_e is equivalent diameter (μm), a is the length of crack (μm), and b is the width of
 476 crack (μm). For the crack shown in Figure 10 the equivalent diameter is roughly equal to 2.53
 477 μm and the effective radius of it is equal to 1.26 μm , which corresponds extremely well to
 478 the effective pore radius of Sample 2 in Table 1 (1.33 μm).

479

480 It is interesting to note that, for porosity and hence, permeability measurement, the
 481 equivalent diameter of cracks is not only depended on dimension of crack but also on flow
 482 properties. So the concept of equivalent diameter was only expressed for comparative
 483 purpose with effective pore radius.

484

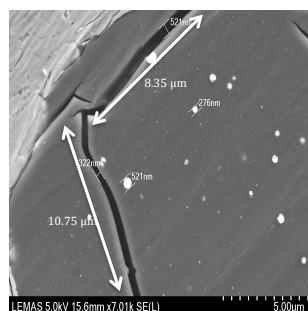
485
486

Figure 9, SEM image of Sample 2 with dimension of crack

487 **Conclusions**

488 X-ray micro-tomography imaging (XRMT) has been used for qualitative and quantitative
489 analysis of the pore structure of gas shale samples, attaining a spatial resolution of 0.9 to 1.2
490 μm . Pore structure can be determined easily using the X-ray tomography technique thanks
491 to the large density contrast between the solid matrix and the pore fluid.

492 The distribution of pore volume showed a great variability of pore scales for all three
493 samples, and different porosities (0.71%, 0.29% and 0.96% for Sample 1, Sample 2 and
494 Sample 3 respectively). These porosities were significantly lower than those obtained on
495 the same samples by MICP measurement. The probable reason for this discrepancy is that the
496 micro-tomography is not taking account of pores on a nanometric scale. Sample 1 was found
497 to have a narrow range of pore aspect ratios, centred on 0.55, with the pores being well
498 aligned in a preferential direction, parallel to the bedding, while Sample 2 and 3 have a much
499 wider range of aspect ratios, encompassing near-spherical pores and thin cracks, centred on
500 0.6, *i.e.*, close to the value for Sample 1. By contrast Sample 3 showed a less clear
501 orientation of the pores. The surface area to volume ratio and permeability were calculated
502 for all three samples.

503 Consideration of the porosity, pore size distributions, pore aspect ratio distributions,
504 pore orientations and surface area to volume ratios as well as the calculated permeabilities
505 shows Sample 1 to be the shale with the most shale gas potential.

506 Shale contains a wide range of pore sizes ranging from hundreds of microns down to
507 a few nanometers (Alfred and Vernik, 2012). The lowest resolution achievable with the X-ray
508 micro-tomographic instrument we used was about one micron. Hence, we expect that we
509 have been analysing only the larger scale subset of the pores in the shale. Measurements
510 are currently underway using an instrument with a nanometer scale resolution in order to
511 ensure all sizes of pores are included in the measurement, and to examine whether the
512 nanometer-scale pores are critical to our understanding of the pore microstructure of gas
513 shale.

514 **Acknowledgments**

515 The authors would like to thank Rodrigo Guadarrama Lara for his great assistance during the
516 use of the X-ray micro-tomography device at Leeds University and the University of Leeds for
517 providing Paul Glover with an academic dowry. We would also like to thank Harri Wyn
518 Williams for his help of sample preparation in Earth and Environment rock preparation
519 laboratory.

520 **References**

- 521
522 1. Alfred, D., & Vernik, L. (2013). A new petrophysical model for organic shales, *Petrophysics*,
523 54(3), 240-247.



- 524 2. Ambrose, R.J., Hartman, R.C., Diaz-Campos, M., Akkutlu, I.Y. and Sondergeld, C.H. (2012).
525 Shale gas-in-place calculations. Part I. New pore-scale considerations: SPE Journal of
526 Petroleum Engineers 17(1), 219-229.
- 527 3. Bahr, K. (1997). Electrical anisotropy and conductivity distribution functions of fractal
528 random networks and of the crust: the scale effect of connectivity. Geophysical Journal
529 International, 130(3), 649-660.
- 530 4. Bakke S., and Øren, P.E. (1997). 3-D Pore-Scale modelling of sandstones and flow simulations
531 in the pore networks: SPE Journal of Petroleum Engineers, 2(02), 136-149.
- 532 5. Blunt M., Bijeljic, B., Dong, H., Gharbi, Q., Iglauer, S., Mostaghimi, P., Paluszny, A., and
533 Pentland, C. (2013). Pore-scale imaging and modeling: Advances in Water Resources, 51,
534 197-216.
- 535 6. Buades, A., Coll, B., and Morel, J.M. (2011). Non-local means denoising: Image Processing On
536 Line, 1, http://dx.doi.org/10.5201/ipol.2011.bcm_nlm
- 537 7. Chalmers, G.R., Bustin, R.M. and Power, I.M. (2012). Characterization of gas shale pore
538 systems by porosimetry, pycnometry, surface area, and field emission scanning electron
539 microscopy/ transmission electron microscopy image analyses: Examples from the Barnett,
540 Woodford, Haynesville, Marcellus, and Doig units. AAPG Bulletin, 96(6), 1099-1119.
- 541 8. Curtis M.E., Ambrose, R.J., Sondergeld, C.H. and Rai, C.S. (2010). Structural characterization
542 of gas shales on the micro- and nano-scales: Paper SPE-137693-MS presented at the SPE
543 Canadian Unconventional Resources and International Petroleum Conference., Calgary,
544 Canada, 19-21 October 2010.
- 545 9. Edwards K., 2015. Unconventional reserves estimation with IHS Harmony, Principal Technical
546 Analyst [online] Available at: [http://blog.ihs.com/rpe-unconventional-reserves-estimation-](http://blog.ihs.com/rpe-unconventional-reserves-estimation-with-ihs-harmony)
547 [with-ihs-harmony](http://blog.ihs.com/rpe-unconventional-reserves-estimation-with-ihs-harmony).
- 548 10. Geng, L., Li, G., Zitha, P., Tian, S. and Sheng, M. (2016). A fractal permeability model for shale
549 gas flow through heterogeneous matrix systems. Journal of Natural Gas Science and
550 Engineering, 35, 593-604
- 551 11. Gerke, K.M., Vasilyev, R.V., Korost, D.V., Karsanina, M.V., Balushkina, N.S., Kalmykov, G.A.
552 and Mallants, D. (2013). Determining Physical Properties of Unconventional Reservoir Rocks:
553 from Laboratory Methods to Pore-Scale Modeling. Society of Petroleum Engineers. SPE
554 167058, doi:10.2118/167058-MS
- 555 12. Glover P.W.J. (2009). What is the cementation exponent? A new interpretation: The Leading
556 Edge, January 2009, 82-85.
- 557 13. Glover P.W.J. (2010). A generalised Archie's law for n phases: Geophysics, 75(6), E247-E265,
558 doi: 10.1190/1.3509781.
- 559 14. Glover, P.W.J., Gómez, J.B. and Meredith, P.G. (2000). Fracturing in saturated rocks
560 undergoing triaxial deformation using complex electrical conductivity measurements:
561 Experimental study. Earth and Planetary Science Letters, 183(1-2), 201-213
- 562 15. Glover P.W.J. (2015). Geophysical Properties of the Near Surface Earth: Electrical Properties,
563 In: Gerald Schubert (editor-in-chief) Treatise on Geophysics, 2nd edition, Vol 11. Oxford:
564 Elsevier, 89-137.
- 565 16. Glover, P.W.J., and Walker, E. (2009). A grain size to effective pore size transformation
566 derived from an electro-kinetic theory, Geophysics, 74(1), E17-E29.
- 567 17. Glover, P.W.J., and Déry, N. (2010). Dependence of streaming potential on grain diameter
568 and pore radius for quartz glass beads, Geophysics, 75(6), F225-241, doi: 10.1190/1.3509465
- 569 18. Henk G. M. (2009). Particle Size Measurements: Fundamentals, Practice, Quality. Springer.
570 pp. 15
- 571 19. Iglauer S., Paluszny, A. and Blunt, M.J. (2013). Simultaneous oil recovery and residual gas
572 storage: A pore-level analysis using in situ X-ray micro-tomography: Journal of Fuel 103, 905-
573 914.
- 574 20. Jennings, B., and Parslow, K. (1988). Particle Size Measurement: The Equivalent Spherical
575 Diameter. Proceedings of the Royal Society of London. Series A, Mathematical and Physical
576 Sciences, 419(1856), 137-149. Retrieved from <http://www.jstor.org/stable/2398336>
- 577 21. Johnson D.L., Koplik, J. and Schwartz, L.M. (1986). New pore-size parameter characterizing
578 transport in porous media: Physical Review Letters, 57(20), 2564-2567,
579 <http://dx.doi.org/10.1103/PhysRevLett.57.2564>



- 580 22. Li, B., Liu, R. and Jiang, Y. (2016). A multiple fractal model for estimating permeability of dual-
581 porosity media. *Journal of Hydrology*, 540, 659-669.
- 582 23. Li, G.G., Diaz, E., & Nur, A. M. (2010). Rock Physical Properties Computed from Digital Core
583 and Cuttings with Applications to Deep Gas Exploration and Development. Society of
584 Petroleum Engineers. doi:10.2118/131601-MS
- 585 24. Loucks, R.G., Reed, R.M., Ruppel, S.C. and Jarvie, D.M. (2009). Morphology, genesis, and
586 distribution of nanometer-scale pores in siliceous mudstones of the mississippian barnett
587 shale. *Journal of Sedimentary Research*, 79(12), 848-861.
- 588 25. Markowicz, A.A. (1993). X-ray physics. *Handbook of X-ray Spectrometry*, 14, 1-28.
- 589 26. Mayo, S., Josh, M., Nesterets, Y., Esteban, L., Pervukhina, M., Clennell, M.B., Maksimenko, A.
590 and Hall, C. (2015). Quantitative micro-porosity characterization using synchrotron micro-CT
591 and xenon K-edge subtraction in sandstones, carbonates, shales and coal. *Fuel*, 154, 167-173.
- 592 27. Mersereau R.M. and Dudgeon D.E. (1975). Two-dimensional digital filtering. *Proceedings of*
593 *the IEEE*, 63, 610-623.
- 594 28. Miller R. G., and Steven R. S. (2014). The Future of Oil Supply. *Mathematical, physical, and*
595 *engineering sciences*.
- 596 29. Nolte, D.D., Pyrak-Nolte, L.J. and Cook, N.G.W. (1989). The fractal geometry of flow paths in
597 natural fractures in rock and the approach to percolation. *Pure and Applied Geophysics*
598 *PAGEOPH*, 131(1-2), 111-138.
- 599 30. Ogilvie, S.R., Orribo, J.M., and Glover, P.W.J. (2001). The influence of deformation bands
600 upon fluid flow using profile permeametry and positron emission tomography: *Geophysics*
601 *Research Letters*, 28(1), 61-64.
- 602 31. Ogilvie, S.R., Isakov, E. and Glover, P.W.J. (2006). Fluid flow through rough fractures in rocks.
603 II: A new matching model for rough rock fractures. *Earth and Planetary Science Letters*,
604 241(3-4), 454-465.
- 605 32. Panahi H., Kobchenko, M., Renard, F., Mazzini, A., Scheibert, J., Dysthe, D., Jamtveit, B.,
606 Malthe-Sorensen, A. and Meakin, P. (2014). A 4D synchrotron X-ray tomography study of
607 the formation of hydrocarbon migration pathways in heated organic-rich shale, *SPE Journal*
608 *of Petroleum Engineers*, 18(02), 366-377.
- 609 33. Peng S.H., Hu, O., Dultz, S. and Zhang, M. (2012). Using X-ray computed tomography in pore
610 structure characterization for a Berea sandstone: Resolution effect: *Journal of Hydrology*,
611 472, 254-261.
- 612 34. Peng, S., Yang, J., Xiao, X., Loucks, B., Ruppel, S.C. and Zhang, T. (2015). An Integrated
613 Method for Upscaling Pore-Network Characterization and Permeability Estimation: Example
614 from the Mississippian Barnett Shale. *Transport in Porous Media*, 109 (2), 359–376.
- 615 35. Passey, Q. R., Bohacs, K., Esch, W. L., Klimentidis, R., & Sinha, S. (2010). From Oil-Prone
616 Source Rock to Gas-Producing Shale Reservoir - Geologic and Petrophysical Characterization
617 of Unconventional Shale Gas Reservoirs. Society of Petroleum Engineers.
618 doi:10.2118/131350-MS
- 619 36. Reipe L., and Suhaimi, M.H.B. (2011). Application of high resolution micro-CT imaging and
620 pore network modeling (PNM) for the petrophysical characterisation of tight gas reservoir –
621 A case history from a deep clastic tight gas reservoir in Oman: Paper SPE-142472-MS
622 presented at the SPE Middle East Unconventional Gas Conference and Exhibition. Muscat,
623 Oman, 31st January – 2nd February, 2011.
- 624 37. Revil, A., and Cathles, L.M. (1999). Permeability of shaly sands: *Water Resources Research*,
625 35(3), 651-662.
- 626 38. Richardson, N. and Gottlieb, M. (2013). The state of shale gas regulation. *Resource for the*
627 *future*, 16, 31-39.
- 628 39. Saleh A., and Castagna, J.P. (2004). Revisiting the Wyllie time average equation in the case of
629 near-spherical pores: *Journal of The Society of Exploration Geophysicists*, 69 (1), 45-55.
- 630 40. Schieber, J. (2010). Common Themes in the Formation and Preservation of Intrinsic Porosity
631 in Shales and Mudstones - Illustrated with Examples Across the Phanerozoic. Society of
632 Petroleum Engineers. doi:10.2118/132370-MS
- 633 41. Sondergeld C.H., Ambrose, R.J., Rai, C.S. and Moncrieff, J. (2010). Micro-structural studies of
634 gas shales: Paper SPE-131771-MS presented at the SPE Unconventional Gas Conference,
635 Pittsburgh, Pennsylvania, USA, 23-25 February 2010.



- 636 42. Tissot B.P. and. Welte, D.H. (1978). Petroleum Formation and Occurrence. A new Approach
637 to Oil and Gas Exploration. XVIII. Berlin-Heidelberg-New York 1978.
638 43. Vernik, L. and Liu, X. (1997). Velocity anisotropy in shales: A petrophysical study. Geophysics,
639 62, 521-532.
640 44. Ward, J. (2010). Kerogen density in the Marcellus shale, Society of Petroleum Engineers, SPE-
641 131767-MS, doi: 10.2118/131767-MS